ab initio statistical mechanics of the ferroelectric phase transition in $PbTiO_3$

U. V. Waghmare† and K. M. Rabe

Dept of Applied Physics, Yale University

P. O. Box 208284, New Haven, Connecticut, 06520-8284

(February 8, 2008)

Abstract

An effective Hamiltonian for the ferroelectric transition in $PbTiO_3$ is constructed from first-principles density-functional-theory total-energy and linear-response calculations through the use of a localized, symmetrized basis set of "lattice Wannier functions." Explicit parametrization of the polar lattice Wannier functions is used for subspace projection, addressing the issues of LO-TO splitting and coupling to the complementary subspace. In contrast with ferroelectric $BaTiO_3$ and $KNbO_3$, we find significant involvement of the Pb atom in the lattice instability. Monte Carlo simulations for this Hamiltonian show a first-order cubic-tetragonal transition at 660 K. Resulting temperature dependence of spontaneous polarization, c/a ratio and unit-cell volume near the transition are in good agreement with experiment. Comparison of Monte Carlo results with mean field theory analysis shows that both strain and fluctuations are necessary to produce the first order character of this transition.

77.80.Bh, 63.20.Dj ,63.70.th, 31.15.Ar

I. INTRODUCTION

Perovskite-structure oxides exhibit various types of lattice instabilities resulting from inherent structural frustration in the prototype cubic structure[1], shown in Fig. 1(a). This class of materials includes a large number of ferroelectrics, with uniform polar distortions and accompanying lattice relaxation (eg. $PbTiO_3, BaTiO_3, KNbO_3$), while cation substitution can result in dramatic changes in ground state distortion (eg. antiferroelectric in $PbZrO_3$, antiferrodistortive in $SrTiO_3$) and corresponding complexities in the mixed systems (eg. $PbZr_{1-x}Ti_xO_3, Ba_{1-x}Sr_xTiO_3$). However, in nearly all examples, the amplitudes and energies of the distortions are rather small, and cubic symmetry is restored at temperatures above a critical temperature T_c, typically a few hundred degrees Kelvin.

For a better understanding of structural phase transitions in perovskite oxides, including chemical trends in the transition temperatures, the first-order vs second-order character of transitions, the relationship between local distortions and average crystallographic structure, and the stability of intermediate temperature phases, first-principles calculations offer valuable access to microscopic information. With advances in algorithms and computational capabilities, the challenge of achieving the high accuracy necessary for studying these distortions has been largely met, and ground state distortions well reproduced for a wide range of perovskite-structure oxides[2–4]. However, for ab initio molecular dynamics or Monte Carlo, the system sizes required for the study of finite-temperature structural transitions are still completely impractical.

An alternative approach is to focus on a restricted subset of the degrees of freedom that is relevant to the transition and construct a simple effective Hamiltonian in this subspace. The parameters in these models are chosen to reproduce the low energy surface of an individual material, and thus to reproduce its finite temperature behaviour in the vicinity of its transition. Comparison of these models gives a systematic understanding of similarities and differences in the microscopic structural energetics of different materials. From the dependence of calculated properties on effective Hamiltonian parameters, one can

also obtain a better understanding of the role of various microscopic couplings in producing the observed behaviour. Microscopic effective Hamiltonians for structural transitions in perovskites were first constructed using the concept of local modes, with empirically determined parameters.[5,6] First-principles total energy calculations were used in the determination of a local mode effective Hamiltonian for the structural transition in $GeTe$[7] and more recently for the structural transitions in $PbTiO_3$[8], $BaTiO_3$[9] and $SrTiO_3$[10]. A systematic approach which generalizes and refines the local mode concept, allowing the efficient construction of an optimal effective Hamiltonian from first-principles total-energy and linear response techniques, has been developed based on the concept of lattice Wannier functions.[11] This approach exploits symmetry properties of the system and is generally applicable to complex structural transitions involving several unstable modes including ones at the zone boundary. Information from additional first principles calculations allows for a systematic check on the validity of the truncation of the effective Hamiltonian, and, when needed, the expansion of the subspace and refinements of its form. The resulting effective Hamiltonian is quantitatively realistic while retaining a simple and physically transparent form.

In this paper, we present a detailed description of the first-principles investigation of $PbTiO_3$[12], which exhibits a single first-order transition at 763 K from the cubic high-temperature phase to the ferroelectric tetragonal ground state, shown in Fig. 1(b). We construct an effective Hamiltonian for this structural phase transition from first principles using the lattice Wannier function method. In contrast with $BaTiO_3$[9] and $KNbO_3$[13] for which the uniform polar distortions in the low temperature phase consist of predominantly B-atom displacements, those in $PbTiO_3$ are dominated by A-atom (Pb) displacements, which will be important in determining the effective Hamiltonian subspace. The effective Hamiltonian also contains the coupling of these local polar distortions to strain. In Ref. 2, the tetragonal phase in $PbTiO_3$ was found to be stabilized relative to the rhombohedral phase by the unit cell relaxation. In addition, we will find that strain plays a crucial role in producing the correct finite temperature transition behaviour.

In Section IIA, we briefly review the method of lattice Wannier functions. In Section IIB

and IIC, the first principles methods and results obtained for the lattice constant, elastic constants, phonon frequencies and the effective charges of $PbTiO_3$ are presented. In Sections IIIA and IIIB, we describe the construction of the effective Hamiltonian, with particular attention to the treatment of LO-TO splitting and crossing of branches through explicit parameterization of the lattice Wannier functions. In Section IIIC, we describe properties of the ground state of the effective Hamiltonian determined from first principles. In Section IV, we present results of finite temperature analysis of H_{eff} using mean field theory and Monte Carlo simulations. These results are discussed in Section V.

II. METHOD

A. Lattice Wannier Function method for the construction of H_{eff}

In the lattice Wannier function method, the effective Hamiltonian is obtained as the result of projection of the full lattice Hamiltonian (in the Born-Oppenheimer approximation) into a subspace of the full ionic displacement space. The effective Hamiltonian subspace is spanned by an orthonormal basis of "lattice Wannier functions:" symmetrized localized atomic displacement patterns taken with respect to a high-symmetry reference configuration. This basis defines a set of coordinates such that a given set of values of the coordinates corresponds directly to a particular pattern of atomic displacements. As a result of the symmetrized and localized nature of the basis, the Taylor expansion of the effective Hamiltonian around the high-symmetry reference configuration (with all coordinate values equal to zero) has a simple form with relatively few parameters, which can be determined from first principles calculations using the correspondence to patterns of atomic displacements.

We briefly review the procedure; further details can be found in Ref. 11. Construction of the subspace begins with a Taylor expansion of the full lattice Hamiltonian to quadratic order. A subset of the eigenvectors of the quadratic Hamiltonian is selected for inclusion in the subspace. This subset must include the unstable modes which freeze in to produce the

low-temperature structure. In addition, to achieve a good description of the branches which emanate from the unstable modes, "end-points" of these branches at high symmetry k-points are included. The symmetry properties of the subspace are established by identifying symmetries of localized functions (Wyckoff position and site symmetry group irrep) which can build up the selected subset of modes.

We follow the prescription in Ref. 11 to obtain an explicit, though approximate, form of a lattice Wannier basis vector. This involves finding the symmetric coordination shells surrounding a representative Wyckoff site and identifying the independent displacement patterns of each shell that transform according to the given irreducible representation of the site symmetry group. The amplitudes of these displacement patterns completely specify an LWF. Because of the localized nature of LWFs, this infinite number of parameters can, to a good approximation, be reduced to a small finite number by neglecting the displacements of shells beyond a chosen range. At high symmetry points in the BZ, the modes built up with these parametrized LWFs are then fit to the corresponding normalized mode eigenvectors obtained from first principles.

These basis functions completely specify the effective Hamiltonian subspace. In the ideal case, this subspace is completely decoupled at quadratic order from its complementary subspace and to a good approximation at higher order as well. This happens when the subspace consists of entire branches isolated in energy from the others and contains all the unstable modes. In most real systems, branches emanating from the unstable modes cross with branches in the complementary subspace. This leads to some degree of quadratic coupling which is unimportant if the crossing occurs far away from the unstable modes. If not, the subspace should be expanded to include these branches. In addition, in polar crystals, the electric field at $\vec{q} \rightarrow 0$ can mix the LO modes differently from the corresponding TO modes. In such a case, the Wannier basis vector which reproduces a given TO branch will not reproduce any LO mode exactly. However, since LO modes are typically high in energy, this approximate description of the LO mode should be adequate for the description of the structural transition.

The quadratic part of the lattice Hamiltonian has both kinetic and potential energy contributions. However, in the classical statistical mechanical treatment, the kinetic energy terms appear in Gaussian integrals in the partition function, factoring out to give a trivial contribution to the free energy. In this case, the eigenmodes used in the construction above could be of either the force constant matrix or the dynamical matrix. In $PbTiO_3$, we have found that the difference in the resulting effective Hamiltonian subspace is rather small and both choices should give comparable results. In the construction described in section III, we have used the eigenmodes of the force constant matrix. Eigenmodes of the dynamical matrix are strongly preferable only if the effective Hamiltonian is also to be used in classical dynamics or quantum mechanical simulations, since in that case the form of the kinetic energy is greatly simplified.

In the final step, the lattice Hamiltonian is projected into this subspace to obtain the effective Hamiltonian. An explicit form H_{eff} is obtained by identifying a small number of physically important terms in a Taylor expansion in the lattice Wannier coordinates. The coefficients of these terms are parameters to be determined from first principles by fitting H_{eff} to the results of selected total energy and linear response calculations, using the explicit correspondence between the Wannier coordinates and the actual ionic displacements. To check the validity of the truncated form of the effective Hamiltonian, additional independent first principles calculations can be performed and compared with H_{eff}.

B. First principles total energy calculations

The first-principles calculations for $PbTiO_3$ were performed using the ab initio pseudopotential method in the local density approximation (LDA) with the Perdew-Zunger parametrization of the Ceperley-Alder density functional.[14] For Pb, the scalar-relativistic pseudopotentials from Ref. 15 were used. The use of a plane wave basis set dictates the use of optimized pseudopotentials[16] for O and Ti to achieve reasonable energy convergence and transferability. For O, the reference configuration $2s^2 2p^4$ was used with pseudopotential

core radii $r_{c,s} = r_{c,p} = 1.5\ a.u.$ Optimization was performed with $q_{c,s} = 7.0(Ry)^{1/2}$ and $q_{c,p} = 6.5(Ry)^{1/2}$ and 4 and 3 Bessel functions for s and p orbitals respectively. For Ti, it is essential to treat the semi-core $3s$ and $3p$ electrons as valence electrons[3,17]. The reference configuration $3s^2 3p^6 3d^2$ was used with pseudopotential core radii $r_{c,s} = r_{c,p} = 1.45\ a.u.$ and $r_{c,d} = 1.5\ a.u.$. Optimization was performed with $q_{c,s} = 7.2(Ry)^{1/2}$, $q_{c,p} = 7.0(Ry)^{1/2}$ and $q_{c,d} = 7.74(Ry)^{1/2}$, and 4 Bessel functions. An energy cutoff of 850 eV (corresponding to approximately 3600 plane waves for a 5-atom unit cell) was used to ensure convergence within $10mRy$/atom. The self-consistent total energy calculations were performed using the program CASTEP 2.1[18] based on the stable and efficient preconditioned conjugate-gradients method[19]. For the Brillouin zone integrations, k-point sampling was performed using the Monkhorst-Pack construction[20] with 64 k-points in the full Brillouin zone.

As reported in Ref. 8 and summarized here in Table (I), the lattice constant and elastic constants of $PbTiO_3$ in the cubic perovskite structure obtained from the total energy calculations for a range of unit cell volumes are in good agreement with previous calculations[2,3]. In addition, in Fig. 4 of Ref. 8 we showed the calculated energies as a function of experimental soft mode amplitude, which compare favorably with previous LAPW calculations[2].

C. First principles DFT linear response

The technique of DFT linear response is used to calculate the second derivatives of the total energy with respect to perturbation parameters through the self consistent calculation of the first order correction to the occupied Kohn-Sham wave functions[21,22]. For example, Born effective charges, dielectric constant and dynamical matrices are the second derivatives of total energies and thus can be obtained with this technique. In this framework, the dielectric constant can be calculated avoiding cumbersome sums over unoccupied bands. Another significant advantage is that $\vec{q} \neq 0$ force constants can be computed with an effort similar to that of a single unit cell total energy calculation.

Our implementation is a modification of CASTEP 2.1 based on the variational formula-

tion of DFT linear response[22]. All the linear response calculations reported here were done at the experimental lattice constant[23] of $3.96883\mathring{A}$ with 64 Monkhorst-Pack k-points in the full Brillouin zone. The Vosko-Wilk-Nusair parametrization of the Ceperly-Alder density functional was used to permit the calculation of derivatives of exchange-correlation terms[24]. A $36 \times 36 \times 36$ fourier transform grid is used for integration over a unit cell in real space. This real space grid breaks global translational invariance[25,22], which manifests itself as small violations of the acoustic sum rule (the calculated frequencies of zone center acoustic modes are not exactly zero) and charge neutrality (the calculated change in polarization due to a rigid displacement of the crystal in any direction is not exactly zero). The acoustic sum rule was imposed by adding small corrections to the diagonal elements of the $\vec{q} = 0$ force constant matrix. Charge neutrality was imposed by adding the same small correction to the effective charges of all atoms.

The Born effective charges are presented in Table (II) in very good agreement with previously calculated values[26]. The main features of interest are the anomalously large effective charges of Ti and O along the bond and the anisotropy of the oxygen charge. The calculated dielectric constant is 8.24, which can be compared with the experimental value of 8.64 quoted in Ref. 26. The data in Table (II) combined with the calculated force constants at $\vec{q} = 0$ give the frequencies of IR-active phonons presented in Table (III). Direct comparison of these results with the previous calculations[26] is not possible because the calculations were performed at different lattice constants. This has an especially large impact on the unstable mode frequency, as confirmed by our calculations of coupling between this mode and homogeneous strain, to be described below. As can be seen in Table (IV), the unstable Γ_{15} mode has the largest mode effective charge, which should be associated with the largest LO-TO splitting. Since there are three polar zone center modes with the same symmetry, mixing leads to LO-mode eigenvectors different from TO-mode eigenvectors. Effects of this mixing can be quantified using the correlation matrix[26]

$$c_{ij} =< \xi_i^{TO} | M | \xi_j^{LO} >, \tag{2.1}$$

given in table (IV), where $M_{mn} = M_m \delta_{mn}$ is the mass matrix and ξ_i are the IR-active mode eigenvectors. As expected, the unstable Γ_{15} TO mode has the strongest correlation with the highest LO mode.

In Table V, we report selected phonon frequencies at other high symmetry k-points in the Brillouin zone, focusing in particular on the lowest energy phonons. While we also find unstable modes away from the Γ point, the unstable mode at Γ is clearly the dominant lattice instability in our calculations, consistent with the observed low-temperature structure. The eigenvectors of the lowest energy phonons and the corresponding force constant matrices will be used in the determination of the parameters in the effective Hamiltonian in the next section.

III. CONSTRUCTION OF THE EFFECTIVE HAMILTONIAN FOR $PBTIO3$

A. Construction of the subspace

The construction of the effective Hamiltonian subspace begins with consideration of the calculated force constant matrix eigenvalues and eigenvectors at Γ, R, M and X. The subspace has to include the unstable polar Γ_{15} mode which freezes in to produce the low temperature tetragonal structure. In addition, to achieve a good description of branches which emanate from this dominant unstable mode, the endpoints of these branches R_{15}, M_2', M_5', X_5' are included. As can be seen from Table (I) of Ref. 11, the lattice Wannier functions which can build up this subset of modes transform like 3-dimensional vectors centered at Pb-sites. It should be noted that the lowest mode at R is actually R_{25}, which corresponds to an oxygen octahedron rotation instability seen in many perovskite oxides[10]. Since crossing of the lowest branch along (111) with that emanating from R_{25} occurs far from the relevant mode Γ_{15} and relatively higher in energy, we do not include it in the subspace.

To include coupling of the relevant polar distortions (Γ_{15}) to local distortions of the unit cell (inhomogeneous strain), we expand the subspace to include the acoustic modes by

choosing an additional set of lattice Wannier functions. Of the three possibilities (listed in Table (I) of Ref. 11), Ti-centered 3-dimensional vectors are preferable to $O_{x,x}$ (1-dimensional vectors) and $O_{x,y}$ (2-dimensional vectors), since this choice corresponds to the smallest subspace expansion and highest site symmetry group. Furthermore, unlike $O_{x,x}$, the resulting $6 \cdot N$ dimensional subspace does not include the highest energy modes.

Next, we obtain an explicit form for the Pb-centered LWF. This involves finding the symmetric coordination shells surrounding a Pb site and identifying the independent displacement patterns of each shell that transform according to the vector representation of the site symmetry group O_h. For a given shell there can be more than one pattern of displacements with a given transformation property. To each such pattern corresponds an independent amplitude parameter. By neglecting the displacements of shells beyond 1st neighbour Ti and O shells and 2nd neighbour Pb shells, we obtain a total of 10 parameters. The first shell of Ti atoms has 2 independent displacement patterns, parametrized by t_1 and t_2; there are 1, 2, 2 parameters for the zeroth, first and second shells of Pb atoms respectively and 3 parameters for the first shell of oxygen atoms. These displacement patterns are shown in Fig. 2.

To determine the numerical values of these parameters for $PbTiO_3$, we build up the transverse modes $e_{\vec{q},\alpha}$ at high symmetry k-points in the Brillouin zone, namely Γ, X, M, and R, from the parametrized LWF using

$$e_{\vec{q},\alpha} = \sum_{\vec{R}_i} exp(i\vec{q} \cdot \vec{R}_i) w_{i,\alpha} \tag{3.1}$$

where $\vec{R}_i$ is a direct lattice vector and $w_{i,\alpha}$ is an LWF centered at the Pb site in the ith unit cell, α being its Cartesian component. This specifies atomic displacements in these modes as linear functions of the parameters, to be fit to the normalized eigenvectors of the force constant matrix calculated from first principles. With the parameters listed above, we can reproduce the normalized eigenvectors of the modes Γ_{15}, R_{15} and M_2' exactly. The remaining free parameters, associated with Pb and Ti displacements, were used to fit to a normalized mode with maximum overlap with the lowest M_5' (see Table (VI)). Numerical values of these

parameters, listed in Table (VII), clearly show that the magnitude of the parameters decays rapidly with shell-radius, confirming the assumption of LWF localization. Furthermore, by adding an additional shell of Pb (one parameter) and oxygen atoms (two parameters), we can reproduce all the transverse optical modes in the subspace. The parameter values for this refined LWF are given in Table (VII). The values of the parameters of the innermost shells do not change very much, and the values of the new parameters are very small.

Another way of testing the approximate LWF is to see how well it reproduces other modes in the subspace. For example, in Table VIII, we show the comparison of the first principles X_5' eigenvector with the mode constructed with the approximate LWF. The approximate mode has an overlap of 92% with the relevant mode, and if the approximate mode vector is normalized, the overlap becomes 99.96%, showing that the LWF describes the subspace very well.

For the simplest treatment of inhomogeneous strain (the acoustic branches), an explicit expression of the Ti-centered LWF is not needed, since the goal is only to reproduce the long wavelength acoustic modes, whose dispersion is determined from the elastic constants. For a more refined treatment, an LWF could be parametrized as above and determined by fitting to the first principles eigenmodes Γ_{15}, R_{25}', M_3', M_5', X_1, X_5.

B. Determination of parameters in H_{eff}

Using the symmetry properties of the lattice Wannier basis for the effective Hamiltonian subspace, we write an explicit expression for H_{eff} as a Taylor expansion in the lattice Wannier coordinates, invariant under the space group $Pm3m$. $\{\vec{\xi}_i\}$ and $\{\vec{u}_i\}$ denote the Pb-centered and Ti-centered lattice Wannier coordinates respectively. Each of these three dimensional vector degrees of freedom transforms according to the Γ_{15} irrep of the point symmetry group O_h. Below, we organize the terms in the expansion of H_{eff} into those acting exclusively in the Pb-centered subspace and the Ti-centered subspace and those coupling the two.

In the Pb-centered subspace, we consider quadratic interactions up to third nearest neighbour with the most general form allowed by the space group symmetry:

$$\begin{aligned}
&\sum_i (A|\vec{\xi_i}|^2 \\
&+\sum_i \sum_{\hat{d}=nn1} [a_L(\vec{\xi_i}\cdot\hat{d})(\vec{\xi_i}(\hat{d})\cdot\hat{d}) + a_T(\vec{\xi_i}\cdot\vec{\xi_i}(\hat{d}) - (\vec{\xi_i}\cdot\hat{d})(\vec{\xi_i}(\hat{d})\cdot\hat{d}))] \\
&+\sum_i \sum_{\hat{d}=nn2} [b_L(\vec{\xi_i}\cdot\hat{d})(\vec{\xi_i}(\hat{d})\cdot\hat{d}) + b_{T1}(\vec{\xi_i}\cdot\hat{d}_1)(\vec{\xi_i}(\hat{d})\cdot\hat{d}_1) + b_{T2}(\vec{\xi_i}\cdot\hat{d}_2)(\vec{\xi_i}(\hat{d})\cdot\hat{d}_2)] \\
&+\sum_i \sum_{\hat{d}=nn3} [c_L(\vec{\xi_i}\cdot\hat{d})(\vec{\xi_i}(\hat{d})\cdot\hat{d}) + c_T(\vec{\xi_i}\cdot\vec{\xi_i}(\hat{d}) - (\vec{\xi_i}\cdot\hat{d})(\vec{\xi_i}(\hat{d})\cdot\hat{d}))], \qquad (3.2)
\end{aligned}$$

where $\vec{\xi_i}(\hat{d})$ denotes the LWF coordinate at a neighbour of site i in $\hat{d}$ direction. Beyond third neighbor we use a dipole-dipole form parametrized by the mode effective charge $\overline{Z}^*$ and the electronic dielectric constant ϵ_∞:

$$\sum_i \sum_{\vec{d}} \frac{(\overline{Z}^\star)^2}{\epsilon_\infty} \frac{(\vec{\xi_i}\cdot\vec{\xi_i}(\hat{d}) - 3(\vec{\xi_i}\cdot\hat{d})(\vec{\xi_i}(\hat{d})\cdot\hat{d}))}{|\vec{d}|^3}. \qquad (3.3)$$

An important simplifying approximation is that the onsite potential, depending on the value of ξ_i at a single i, is the only set of terms including anharmonic interactions acting exclusively in the Pb-centered subspace. For simplicity, anharmonic terms are included only in the onsite potential with isotropic terms up to eighth order in $|\vec{\xi_i}|$ and full cubic anisotropy at fourth order:

$$\sum_i (B|\vec{\xi_i}|^4 + C(\xi_{ix}^4 + \xi_{iy}^4 + \xi_{iz}^4) + D|\vec{\xi_i}|^6 + E|\vec{\xi_i}|^8). \qquad (3.4)$$

In the Pb-centered subspace, the parameters to be determined from first principles are $A, a_L, a_T, b_L, b_{T1}, b_{T2}, c_L, c_T, B, C, D, E, \overline{Z}^\star$. This determination relies on the explicit correspondence between the lattice Wannier coordinate $\{\vec{\xi_i}\}$ and the ionic displacements $\{\vec{d_i}\}$ obtained in subsection III A. This correspondence allows us to relate the first principles total energies and the derivatives of total energies to various terms in H_{eff}. The parameters in the quadratic part of H_{eff} are linearly related to the force constant matrices obtained from density functional linear response at high symmetry k-points in the BZ. In Table (IX) are given specific relations for modes at various k-points in the BZ including $\Gamma_{15}, X_2', X_5', M_5', M_2', R_{15}$

and the Λ_3 modes at $(111)\pi/(2a), (111)\pi/(4a)$. The parameter $\overline{Z}^*$ is determined from the eigenvector of unstable Γ_{15} and the Born effective charges. Obtaining ϵ_∞ directly from DFT linear response and solving the system of linear equations yields values for all the parameters in the quadratic part of H_{eff}, listed in Table (IX). The resulting normal mode dispersion of H_{eff} is shown in Fig. 3. For the LO modes at $(111)\pi/(2a)$ and $(111)\pi/(4a)$, the reasonable agreement between the calculated force constant matrix eigenvalue and H_{eff} is an indication of the validity of the truncation in the Taylor expansion.

The parameters B, C, D, E appearing in the onsite anharmonic terms are determined from the total energies of uniformly distorted configurations ($\vec{\xi_i} = \vec{\xi}$), as shown in Fig. 4. The minimum energy configuration has rhombohedral symmetry ($\vec{\xi}$ along (111)). The difference among the energies of uniform distortions with different symmetries ((100), (110), (111)) is a reflection of the cubic anisotropy, which is described quite well by the fourth order terms. The resulting parameters are listed in Table (X).

To account for the effects of changes in lattice parameters at the structural phase transition, we include the lowest order terms in the homogeneous strain and its coupling to the Pb-centered subspace:

$$\frac{N}{2}C_{11}\sum_\alpha e_{\alpha\alpha}^2 + \frac{N}{2}C_{12}\sum_{\alpha\neq\beta} e_{\alpha\alpha}e_{\beta\beta} + \frac{N}{4}C_{44}\sum_{\alpha\neq\beta} e_{\alpha\beta}^2 + Nf\sum_\alpha e_{\alpha\alpha}$$
$$+g_0(\sum_\alpha e_{\alpha\alpha})\sum_i |\vec{\xi_i}|^2 + g_1\sum_\alpha(e_{\alpha\alpha}\sum_i \xi_{i\alpha}^2) + g_2\sum_{\alpha<\beta} e_{\alpha\beta}\sum_i \xi_{i\alpha}\xi_{i\beta}, \qquad (3.5)$$

where $e_{\alpha\beta}$ is a component of the strain tensor, C_{11}, C_{12}, C_{44} are the elastic constants, and the parameters g_0, g_1, g_2 give the strength of coupling of strain with the local polar distortions $\xi_{i\alpha}$. All these parameters are determined from the single unit cell total-energy calculations for three independent types of unit cell distortions (isotropic, uniaxial and rhombohedral shear), with magnitudes of up to 2 to 4 % of the experimental lattice constants. The total energies of these strained unit cells with no local polar distortion, shown in Fig. 5, give the three elastic constants C_{11}, C_{12} and C_{44}. For each of these unit-cell-strain types, we also compute the second derivative of energy with respect to uniform local polar distortions $\vec{\xi_i} = \vec{\xi}$, as shown in Fig. 5. These results yield the coupling parameters shown in Table (X).

Now we turn to the determination of the terms in H_{eff} acting in the Ti-centered subspace. Because this subspace contains the zone center acoustic modes, these terms must satisfy global translational and rotational invariance. This symmetry is built into the systematic expansion procedure given by Keating[27], in which invariant terms are built up from dot products of differences of the $\vec{u}_i$'s. If the expansion of the effective Hamiltonian in the Keating construction[27] is truncated at quadratic order and three independent parameters, corresponding to the three elastic constants, the following terms are obtained:

$$\frac{1}{N}\sum_i \tilde{A}|\vec{u}_i|^2$$

$$+\frac{1}{N}\sum_i\sum_{\hat{d}=nn1}[\tilde{a}_L(\vec{u}_i\cdot\hat{d})(\vec{u}_i(\hat{d})\cdot\hat{d})+\tilde{a}_T(\vec{u}_i\cdot\vec{u}_i(\hat{d})-(\vec{u}_i\cdot\hat{d})(\vec{u}_i(\hat{d})\cdot\hat{d}))]$$

$$\frac{1}{N}\sum_i\sum_{\hat{d}=nn2}[\tilde{b}_L(\vec{u}_i\cdot\hat{d})(\vec{u}_i(\hat{d})\cdot\hat{d})+\tilde{b}_{T1}(\vec{u}_i\cdot\hat{d}_1)(\vec{u}_i(\hat{d})\cdot\hat{d}_1)+\tilde{b}_{T2}(\vec{u}_i\cdot\hat{d}_2)(\vec{u}_i(\hat{d})\cdot\hat{d}_2)] \qquad (3.6)$$

The relations of these parameters to the elastic constants are made by using the Keating expansion to evaluate the energy of homogeneously strained configurations. With these relations, $\tilde{A}=C_{11}+2C_{44}$, $\tilde{a}_L=-\frac{1}{2}C_{11}$, $\tilde{a}_T=-\frac{1}{2}C_{44}$, $\tilde{b}_L=-\tilde{b}_{T1}=-\frac{1}{8}C_{12}+\frac{1}{24}C_{44}$ and $\tilde{b}_{T2}=0$, these parameters can easily be obtained from first-principles calculations. Because there are no unstable modes in this subspace, there is no need to include higher-order interactions. In any case, within the local anharmonicity approximation, global translational invariance requires anharmonic terms to be zero at all orders. As mentioned in the previous section, there is no need for an explicit form of the Ti-centered LWF in this minimal treatment. For refinement of H_{eff} in this subspace, one could construct an explicit form and determine additional parameters in a manner analogous to that for the Pb-centered subspace.

Finally, the simplest coupling between local polar distortions (Pb-centered subspace) and inhomogeneous strain (Ti-centered subspace) that satisfies the constraint of global translational invariance and does not vanish in the limit $\vec{k}\to 0$ is the nearest-neighbor coupling linear in $\vec{u}$ and quadratic in $\vec{\xi}$, with both $\vec{\xi}$ variables taken on the same site:

$$\frac{\tilde{h}_0}{N}\sum_i\{\xi_{ix}^2\sum_{\vec{d}=\pm\hat{y}\pm\hat{z}}(u_x(\vec{R}_i+\frac{a_0}{2}\hat{x}+\frac{a_0}{2}\vec{d})-u_x(\vec{R}_i-\frac{a_0}{2}\hat{x}+\frac{a_0}{2}\vec{d}))+c.p.\}$$

$$
\begin{aligned}
&+\frac{\tilde{h}_1}{N}\sum_i\{\xi_{ix}^2(\sum_{\vec{d}=\pm\hat{x}\pm\hat{z}}(u_y(\vec{R}_i+\frac{a_0}{2}\hat{y}+\frac{a_0}{2}\vec{d})-u_y(\vec{R}_i-\frac{a_0}{2}\hat{y}+\frac{a_0}{2}\vec{d}))\\
&\quad+\sum_{\vec{d}=\pm\hat{x}\pm\hat{y}}(u_z(\vec{R}_i+\frac{a_0}{2}\hat{z}+\frac{a_0}{2}\vec{d})-u_z(\vec{R}_i-\frac{a_0}{2}\hat{z}+\frac{a_0}{2}\vec{d})))+c.p.\}\\
&+\frac{\tilde{h}_2}{N}\sum_i\{\xi_{ix}\xi_{iy}(\sum_{\vec{d}=\pm\hat{x}\pm\hat{z}}(u_x(\vec{R}_i+\frac{a_0}{2}\hat{y}+\frac{a_0}{2}\vec{d})-u_x(\vec{R}_i-\frac{a_0}{2}\hat{y}+\frac{a_0}{2}\vec{d}))\\
&\quad+\sum_{\vec{d}=\pm\hat{y}\pm\hat{z}}(u_y(\vec{R}_i+\frac{a_0}{2}\hat{x}+\frac{a_0}{2}\vec{d})-u_y(\vec{R}_i-\frac{a_0}{2}\hat{x}+\frac{a_0}{2}\vec{d})))+c.p.\}
\end{aligned}
\tag{3.7}
$$

$\xi_{i\alpha}^2$ couples only to differences of the u_β's, which can be recognized as finite difference approximations to the gradient, and thus as the local strain tensor (see also Ref. 9). The terms in H_{eff} coupling inhomogeneous strain and polar distortions are related in the long wavelength limit to the coupling between homogeneous strain and the polar Γ_{15} mode. Thus the three independent coupling parameters can be obtained from the corresponding homogeneous strain coupling parameters: $\tilde{h}_0=(g_0+g_1)/4, \tilde{h}_1=g_0/4$ and $\tilde{h}_2=g_2/8$.

C. Examination of model energetics

Having fully determined H_{eff}, we now explore the low energy surface of the model to confirm that it gives a correct ground state when compared with the real crystal. Since the anharmonic terms occur only in the Pb-subspace and are local (the anharmonicity is wavevector independent), it is easy to determine the ground state from the quadratic order terms. The lowest energy mode is obtained by freezing in the most unstable mode: Γ_{15}. We consider changes in energy as this mode is frozen in with polarization along the $(001), (110)$ and (111) directions. In Fig. 4, it can be seen that the rhombohedral state ((111)-distortion) has the lowest energy. If the unit cell is allowed to relax as the mode is frozen in, by minimizing over the homogeneous strain, we find an overall increase in distortion energy, with the lowest energy state being of tetragonal symmetry ((001)-distortion) as can be seen in Fig. 6. This is consistent both with previous first principles calculations[2] and experimental results[23].

For the lowest energy tetragonal configuration, we obtain a value for the spontaneous

polarization from the mode effective charge of $P_s = 0.87 C/m^2$, which is in the range of values ($P_s = 50$ to $100 C/m^2$) reported from experiments[1]. From the values of homogeneous strain in this ground state, we obtain a c/a ratio of 1.08, to be compared with the experimental value of 1.061[23]. Using the explicit form for the LWF, the atomic displacements in the model ground state can be obtained. We find that the oxygen octahedra are almost undistorted and the relative displacement of the Pb atoms is 0.35 Å(to be compared with the experimental value of 0.47 Å[23]). It should be noted that this is not the true LDA ground state, since previous total energy calculations[8] for the experimental distortions showed the latter is slightly lower in energy. This means that there is a higher order coupling of the unstable Γ_{15} mode to an additional polar Γ_{15} mode not included in the effective Hamiltonian subspace. Considering that the atomic displacements in $PbTiO_3$ are relatively large, the presence of such anharmonicity is not surprising. However, as discussed above, the ground state of the model is very similar to the experimental ground state and the small loss of accuracy is more than compensated for by the gain in simplicity.

IV. FINITE-TEMPERATURE BEHAVIOUR

The effective Hamiltonian is constructed to show the same finite temperature critical behaviour as the full lattice Hamiltonian in a statistical mechanical analysis. While the form of H_{eff} is somewhat too complicated for the application of analytical methods beyond mean field theory, it is quite suitable for Monte Carlo simulations, since the changes in energy for changing system configurations can be readily evaluated. Monte Carlo simulations are used in the detailed analysis of H_{eff} to obtain T-dependence of a variety of structural properties near the transition, while our mean field theory analysis is limited to the estimation of T_c and the identification of the order of the transition and symmetry of the phases. Comparison of the mean field results with those of Monte Carlo simulations allows us to study the effects of fluctuations.

A. Mean field theory

Variational mean field theory for the class of models with variable length vector degrees of freedom and strain coupling was developed in Ref. 28. In this approach, the homogeneous strain and uniform polarization ($\vec{P}$) are identified as the order parameters for the transition. $\vec{P}$ is directly related to the average value of uniform local distortion through the mode effective charge $\overline{Z}^{\star}$ and the unit cell volume Ω_{cell},

$$\vec{P} = \overline{Z}^{\star}. < \vec{\xi} > /\Omega_{cell}. \tag{4.1}$$

In the high temperature (cubic perovskite) phase, the uniform polarization is zero and the strain tensor has full cubic symmetry: $e_{xx} = e_{yy} = e_{zz}$. We used the variational formulation of mean field theory, which involves constructing a trial density matrix as a product of single site density matrices and minimizing the resulting free energy functional with respect to the variational parameters in the trial density matrix. We minimized the trial free energy with respect to variational parameters corresponding to cubic, tetragonal and rhombohedral symmetries to determine the stable phase at various temperatures. The system is stable in the cubic phase above the transition temperature $T_c = 1100K$ and in the tetragonal phase below T_c, but within the accuracy of our calculation, the transition is second order. Switching off the coupling to homogeneous strain resulted in a second order cubic-rhombohedral transition at a significantly lower temperature of 900 K.

B. Monte Carlo simulations

Classical Monte Carlo simulations[29] were performed using the Metropolis algorithm for finite size systems of $L \times L \times L$ unit cells and periodic boundary conditions. A configuration of the system is specified by two sets of three dimensional vectors $\{\vec{\xi}_i\}$ and $\{\vec{u}_i\}$ placed on interpenetrating simple cubic lattices of size $L \times L \times L$. We generated a trial configuration by updating a single vector to a randomly chosen vector inside a cubic box centered at the current value of the vector. The size of this box is chosen to yield a reasonable acceptance

ratio (> 0.1), and is roughly $0.25a_0$ near T_c. With the change in a single vector, the change in energy associated with short range terms (quadratic interactions up to third neighbour, the onsite potential, coupling to strain and third order coupling between the two subspaces) is easy to calculate. Because of their long range, computation of dipolar intersite interactions is relatively costly, limiting the size of our simulations to $L \leq 12$. The 3×3 matrix of dipolar intersite coupling for each pair of spins was calculated using the Ewald summation technique for each value of L. Changes in the quadratic intersite interaction due to changes in strain are neglected in this model. One Monte Carlo sweep (mcs) involves one update of the ξ_i's (in typewriter mode) followed by one update of the u_i's (in typewriter mode), and 20 updates of the 6 components of the strain tensor.

Preliminary Monte Carlo simulations performed with 25,000 to 50,000 sweeps showed dependence on the initial configuration of simulations at temperatures in the vicinity of the transition for $L > 5$. For $L = 5$, which is small enough for ergodic sampling in a run of this length, the energy histogram shows two clearly separated peaks. This behaviour is typical of a first order transition[30]. At larger system sizes, due to the exponentially increasing free energy barrier between the regions of configuration space corresponding to low and high temperature phases, only one of the two peaks in the energy histogram is sampled, depending on the choice of initial configuration. An accurate determination of T_c requires knowledge of the relative free energies of the high and low temperature phases as a function of temperature. Recently developed methods to extract T_c for first order transitions include multicanonical algorithms[30] and jump-walking algorithms[31]. In our applications of these methods to $PbTiO_3$, we found that these approaches require very long (10^6 mcs) simulations, and therefore are rather impractical. However in the present case, the uncertainty in T_c obtained from the range of hysteresis is small compared to the LDA and other errors in our analysis and therefore high accuracy determination of T_c is not necessary. The calculation of the physical properties of the high and low temperature phases at temperatures inside the range of hysteresis is carried out with an appropriate choice of the initial configuration.

In Fig. 7, we show the bounds on T_c for $L = 5$ through 11, obtained by monitoring the

sensitivity of the average structural parameters to the choice of initial state: $T_>$ is the lowest temperature at which the system averages are characteristic of the cubic state, starting with an inital ground state tetragonal configuration, while $T_<$ is the highest temperature at which a starting cubic configuration results in a tetragonal state. A value of $T_c = 660K$, obtained from averaging the bounds at the largest system size, is in very good agreement with the experimental transition temperature 763K.

To detect the symmetry of the low temperature phase, we calculated the averages of largest, smallest and intermediate absolute values of the cartesian components of $\vec{\xi} = \frac{1}{N}\sum_i(\vec{\xi_i})$. These averages for the $7 \times 7 \times 7$ system as a function of temperature are shown in Fig. 8. Near T_c, the largest component jumps to a finite value, while the other two components remain close to zero, indicating tetragonal symmetry of the low temperature phase. As shown in Fig. 9, this uniform tetragonal polar distortion is accompanied by a tetragonal strain $c/a \neq 1$. This quantity also shows a marked jump near T_c. Finally, from the average homogeneous strain we obtained the average volume of the system as a function of temperature, as shown in Fig. 10. The negative thermal expansion in the simulations just below T_c is also seen experimentally[32].

The latent heat of a first order transition is given by the difference in energies at which the two peaks appear in the energy histogram in the simulations at T_c. To determine this energy difference, we performed two simulations for $L = 9$ at the midpoint of the hysteresis range $T_c = 675K$, one starting with a tetragonal configuration and the other starting with a cubic configuration. The difference in the positions of the peaks in the energy histograms for these two simulations yields an estimate of latent heat of 3400 J/mol, in rough agreement with the measured value of 4800 J/mole[33]. It should be noted that these values are much larger than 209 J/mol latent heat of the cubic tetragonal transition of $BaTiO_3$[34].

Information about the local distortions in the high temperature nonpolar phase just above T_c, can be obtained from the single spin distribution $< \vec{\xi_i} >$. For all L, we find the distribution to be very close to Gaussian. The rather broad width ($\approx 0.04a_0$) shows that there are significant local distortions.

For the system sizes used in the simulations, the coupling to the inhomogeneous strain appears to be relatively unimportant. If the coupling is set to zero the changes in the calculated T_c and other transition properties are negligible. However, for larger scale simulations involving multiple domains the effects should be significant.

V. DISCUSSION

The first principles effective Hamiltonian constructed in the previous section provides a quantitative microscopic description of the structural energetics of $PbTiO_3$ relevant to the paraelectric-ferroelectric phase transition. This model can be used to investigate the connection of specific features of the Hamiltonian to the observed behaviour in the vicinity of the transition. In addition, it is possible to connect these features to aspects of the chemistry of $PbTiO_3$ and related compounds.

One important feature of the Hamiltonian is that the TO branches are unstable throughout most of the BZ (Fig. 3). So, although Γ_{15} is the dominant instability, finite wavelength fluctuations have relatively low energy. This may account for the breadth of the single site distribution, and can be expected also to be reflected in the short range order. The unstable branch along the (111) direction in $PbTiO_3$ is quite flat when compared with $SrTiO_3$[35] and $KNbO_3$[13]. In comparison with $KNbO_3$ and ferroelectric $BaTiO_3$, in which the polar unstable modes have a strong B-component[13,9], the instabilities in $PbTiO_3$ are dominated by large Pb-displacements. From symmetry arguments[11], the Pb displacements couple with oxygen displacements at Γ, X, R and M leading to the low energy of the modes at those points. While the same argument applies to Ti displacements at Γ, X and M, they do not couple with any other mode at R point. Therefore, the energy of the mode at R is high and the dispersion along Γ to R is large. The special role Pb plays in the instabilities of $PbTiO_3$ and $PbZrO_3$[36] in contrast with the A-atoms in non-Pb perovskite compounds has its origin in the strong hybridization of Pb with oxygen atoms[2,37].

To understand the consequences of the coupling of the polar subspace to the strain at

finite temperature, we performed Monte Carlo simulations for H_{eff} with this coupling set to zero. This corresponds to a constant volume phase transition with the unit cell constrained to be cubic. In this case, we find a second order phase transition at 400 K directly to the rhombohedral phase. Thus, the coupling of local polar distortions to strain is responsible for both the stability of the tetragonal phase relative to the rhombohedral one and the first order character of the transition at finite temperature. As discussed in the previous section, mean field theory shows a second order transition both with and without strain coupling, implying that both fluctuations and strain coupling are required for producing the first order transition. Comparing the transition temperatures obtained in Monte Carlo and mean field theory with and without strain coupling, we find that while fluctuations suppress T_c, the coupling to strain enhances the stability of the ferroelectric phase.

In comparison with related ferroelectric compounds, the transition in $PbTiO_3$ has a much stronger first order character, reflected in its large latent heat. While the strain coupling is responsible for the first order character[38], anharmonicity in the lattice plays an important role in the magnitude of its discontinuity[28]. The minimum energy uniform polar distortions in $PbTiO_3$ are much larger than those in related compounds indicating a large contribution from anharmonicity in the low-energy surface. The relation of these features to the chemistry of A or B atoms was discussed using ionic radii in Ref. 28.

There are two main sources of error in the work presented in this paper. One of these is the LDA used in the exchange correlation functional. Equilibrium lattice constants are typically underestimated in the LDA calculations. This can strongly affect the study of structural phase transition, since the lattice instabilities are very sensitive to the lattice parameters. In the present work these errors were partially eliminated by expanding the effective Hamiltonian around the experimental lattice constant near T_c and dropping the term linear in strain. The other source of error is the truncation of the effective Hamiltonian subspace. In the LWF approach, this subspace is decoupled at quadratic order from its complementary subspace to a good approximation. However there can be anharmonic coupling between the two subspaces. In the case of $PbTiO_3$, there is a small higher order

coupling of Γ_{15} to modes not included in the subspace, which affects the energies of large distortions. Since these large distortions are mainly important at low temperatures, we expect this coupling to have a small effect on T_c.

VI. CONCLUSION

In conclusion, we have applied the method of lattice Wannier functions to construct an effective Hamiltonian for the ferroelectric phase transition in $PbTiO_3$ completely from first principles. Monte Carlo simulations for this Hamiltonian yield a first order cubic-tetragonal transition at 660 K and a description of the system near the transition in good agreement with experiment. The strong involvement of Pb atom in the lattice instability as well as anharmonicity and the coupling of polar distortions with homogeneous deformations of the lattice are found to be very important in producing the transition behaviour characteristic of $PbTiO_3$.

ACKNOWLEDGMENTS

We are grateful for useful discussions with R. E. Cohen, E. Cockayne, B. A. Elliott, Ph. Ghosez and Serdar Ogut. We thank M. C. Payne and V. Milman for the use of and valuable assistance with CASTEP 2.1. This work was supported by ONR Grant N00014-91-J- 1247. Part of the calculations were performed at the Cornell Theory Center. In addition, K. M. R. acknowledges the support of the Clare Boothe Luce Fund and the Alfred P. Sloan Foundation.

REFERENCES

† Current address: Dept. of Physics, Harvard University, Cambridge, MA 02138.

[1] M. E. Lines and A. M. Glass, *Principles and Applications of Ferroelectrics and Related Materials* (Oxford, 1977), Chap. 8.

[2] R. E. Cohen and H. Krakauer, Ferroelectrics **136**, 65 (1992).

[3] R. D. King-Smith and D. Vanderbilt, Phys. Rev. **49**, 5828 (1994).

[4] D. J. Singh and L. L. Boyer, Ferroelectrics, **136**, 95 (1992).

[5] E. Pytte, Phys. Rev. **B5**, 3758 (1972); E. Pytte and J. Feder, Phys. Rev. **187**, 1077 (1969); J. Feder and E. Pytte, Phys. Rev. **B1**, 4803 (1970).

[6] M. E. Lines, Phys. Rev. **177**, 797 (1969).

[7] K. M. Rabe and J. D. Joannopoulos, Phys. Rev. Lett. **59**, 570 (1987); Phys. Rev. B **36**, 6631(1987); in "Electronic Phase Transitions", ed. by W. Hanke and Y. V. Kopaev (North-Holland, Amsterdam, 1992), Chap. 3.

[8] K. M. Rabe and U. V. Waghmare, Ferroelectrics **164**, 15 (1995).

[9] W. Zhong, D. Vanderbilt, and K. M. Rabe, Phys. Rev. Lett. **73**, 1861 (1994); Phys. Rev. B **52**, 6301 (1995); W. Zhong and D. Vanderbilt, Phys. Rev. Lett. **74**, 2587 (1995).

[10] W. Zhong and D. Vanderbilt, Phys. Rev. Lett. **74**, 2587 (1995).

[11] K. M. Rabe and U. V. Waghmare, Phys. Rev. B **52**, 13236 (1995).

[12] K. M. Rabe and U. V. Waghmare, to appear in J. Phys. Chem. Sol.

[13] R. Yu and H. Krakauer, Phys. Rev. B**49**, 4467 (1994).

[14] D. M. Ceperley, Phys. Rev. **B18**, 3126 (1978); D. M. Ceperley and B. J. Alder, Phys. Rev.Lett. **45**, 566 (1980); J. Perdew and A. Zunger, Phys. Rev. **B23**, 5048 (1981)

[15] G. B. Bachelet, D. R. Hamann and M. Schluter, Phys. Rev. **B26**, 4199 (1982).

[16] A. M. Rappe, K. M. Rabe, E. Kaxiras and J. D. Joannopoulos, Phys. Rev. **B44**, 1227 (1990); M. P. Teter, Phys. Rev. B **48,** 5031 (1993).

[17] Ph. Ghosez, X. Gonze and J.-P. Michenaud, Ferroelectrics **153**, 19 (1994).

[18] M. C. Payne, X. Weng, B. Hammer, G. Francis, I. Stich, U. Bertram, A. de Vita, J. S. Lin, A. Qteish and V. Milman, Cavendish Laboratory, University of Cambridge.

[19] M. C. Payne, D. C. Allan, T. A. Arias, M. P. Teter and J. D. Joannopoulos, Rev. Mod. Phys. **64**, 1045 (1992).

[20] H. J. Monkhorst and J. D. Pack, Phys. Rev. **B13**, 5188 (1976).

[21] S. Baroni, P. Giannozzi and A. Testa, Phys. Rev. Lett. **58**, 1861 (1987)

[22] X. Gonze, D. C. Allan and M. P. Teter, Phys. Rev. Lett. **68**, 3603 (1992).

[23] G. Shirane, R. Pepinsky and B. C. Frazer, Acta Cryst., **9**, 131 (1956).

[24] S. H. Vosko, L. Wilk and M. Nusair, Can. J. Phys. **58**, 1200 (1980).

[25] P. Giannozzi, S. de Gironcoli, P. Pavone and S. Baroni, Phys. Rev. **B43**, 7231 (1991).

[26] W. Zhong, R. D. King-Smith and D. Vanderbilt, Phys. Rev. Lett. **72**, 3618 (1994).

[27] P. N. Keating, Phys. Rev. **145**, 637 (1966).

[28] K. M. Rabe and U. V. Waghmare, Phil. Trans. Roy. Soc. Lond. A, to be published.

[29] M. P. Allen and D. J. Tildesley, *Computer Simulation of Liquids*, (Oxford, 1987), Chap. 4.

[30] B. A. Berg and T. Neuhaus, Phys. Rev. Lett. **68**, 9 (1992); C. Borgs and W. Janke, Phys. Rev. Lett. **68**, 1738 (1992); W. Janke, Phys. Rev. **B47**, 14757 (1992).

[31] C. J. Tsai and K. D. Jordan, J. Chem. Phys. **99**, 6957 (1993).

[32] M. Adachi, et al., in *Landolt-Börnstein: Numerical data and functional relationships in science and technology,* Vol. III/16a, ed. by K. H. Hellwege and A. M. Hellwege, (Springer, 1981), p. 45.

[33] G. Shirane and E. Sawaguchi, Phys. Rev. **81**, 458 (1951).

[34] G. Shirane and A. Takeda, J. Phys. Soc. Jpn. **7**, 1 (1952).

[35] C. LaSota, C.-Z. Wang, Rici Yu, and H. Krakauer, Fourth Williamsburg Workshop on First-Principles Calculations for Ferroelectrics (1996).

[36] U. V. Waghmare and K. M. Rabe, to appear in Ferroelectrics.

[37] D. Singh, Phys. Rev. **B52** 12559 (1995).

[38] K. M. Rabe and U. V. Waghmare, unpublished.

[39] S. Marais, V. Heine, C. Nex and E. Salje, Phys. Rev. Lett. **66**, 2480 (1991).

[40] S. Padlewski, A. K. Evans, C. Ayling and V. Heine, J. Phys. Cond. Matt. **4**, 4895 (1992).

[41] N. Sicron, B. Ravel, Y. Yacoby, E. A. Stern, F. Dogan and J. J.Rehr, Phys. Rev. **B50**, 13168 (1994).

TABLES

TABLE I. Cubic perovskite lattice and elastic constants calculated from various first principles calculations. Elastic constants are given in eV/cell.

	This work	Ref. 2	Ref. 3
a_0 (Å)	3.883	3.889	3.889
B (GPa)	203	215	209
C_{11}	117.	-	123.
C_{12}	51.6	-	53.6
C_{44}	137.	-	148.

TABLE II. Effective charges calculated from first principles linear response and compared with the results of the geometric phase approach (Ref. 26).

	$Z^\star_{pb}$	$Z^\star_{ti}$	$Z^\star_{o1}$	$Z^\star_{o2}$
This work	3.87	7.07	-5.71	-2.51
Ref. 26	3.90	7.06	-5.83	-2.56

TABLE III. IR active optical phonon frequencies (cm^{-1}) at Γ obtained using linear response at the experimental volume. They are compared with the results of the frozen phonon calculations performed at the LDA volume with ultrasoft pseudopotentials[26].

	TO1	TO2	TO3	LO1	LO2	LO3
Present work	182 I	63	447	47	418	610
Ref. 26	144 I	121	497	104	410	673

TABLE IV. LO-TO splitting: mode effective charges and correlation matrix.

	$\overline{Z}^{\star}$	LO1	LO2	LO3
TO1	9.45	0.224	0.466	0.855
TO2	2.56	0.974	0.116	0.192
TO3	1.53	0.010	0.876	0.481

TABLE V. Selected phonon frequencies (cm^{-1}) at high symmetry k-points calculated using DFT linear response. Symmetry labels follow the convention of Ref. 11.

k-point	phonon	frequencies
X	X_5'	30.6 I, 264
	X_2'	93.1, 647
M	M_5'	35.1 I, 400, 201
	M_2'	16.4
	R_{25}	145 I
	R_{15}	15.5, 339
R	R_{25}'	367
	R_{12}'	370
	R_2'	746
	Λ_1	8.78, 249, 421, 696
$(111)\frac{\pi}{2a}$	Λ_2	148
	Λ_3	58.2 I, 82.9, 230, 301, 430

TABLE VI. Determination of LWF parameters. Linear combinations of these parameters for the modes at high symmetry k-points and the corresponding components of the normalized eigenvectors of the force constant matrix.

Mode	combination of the parameters	component of the eigenvector
Γ_{15}	$p_1 + 4p_2 + 2p_3 + 12p_4$	0.5560
	$8t_1$	0.5375
	$4o_1$	-0.3414
	$4o_2$	-0.4109
R_{15}	$p_1 - 4p_2 - 2p_3 + 12p_4$	0.8981
	$4o_3 - 8o_6$	-0.3110
M_2'	$p_1 - 4p_2 + 2p_3 - 4p_4$	1.0000
M_5'	$p_1 - 2p_3 - 4p_4$	0.9010
	$8t_2$	0.3024

TABLE VII. Values of the LWF parameters determined from first principles. The parameters of the approximate LWF described in the text are given in the second column. Parameters for the refined LWF are obtained by fitting to all the TO modes at Γ, R, X and M, with additional parameters associated with third neighbour shell of Pb atoms and second neighbour shell of oxygen atoms.

Parameter	Approx. LWF	Refined LWF
p_1	0.839	0.829
p_2	-0.037	-0.049
p_3	-0.012	0.014
p_4	-0.009	-0.019
p_5	0.0	0.017
o_1	-0.085	-0.086
o_2	-0.102	-0.103
o_3	-0.077	-0.087
o_4	0.	.00045
o_5	0.	-.0045
t_1	0.067	0.067
t_2	0.038	0.037

TABLE VIII. Comparison of X_5' eigenvectors. Mode vector (first row) built up using the approximate LWF is compared with the eigenvector (second row) of the force constant matrix at X.

	Pb component	O component
Mode in the subspace	0.853	-0.341
Eigenvector from LR	0.937	-0.349

TABLE IX. Determination of coefficients in the quadratic part of H_{eff}. Linear combinations of these coefficients for the modes in the H_{eff} subspace at high symmetry k-points are equated to the corresponding eigenvalues of the projected force constant matrix.

k-point	Mode eigenvalue at k of the effective Hamiltonian	Value from LR ($eV/\mathring{A}^2$)
-	$z = \overline{Z}^{\star 2}/\epsilon_\infty$	12.18
Γ_{15}	$A + 2(a_L + 2a_T) + 4(b_L + b_{T1} + b_{T2}) + 8(c_L + 2c_T)/3 - 0.964843z/2$	-1.908
X_2'	$A - 2a_L + 4a_T - 4(b_L + b_{T1}) + 4b_{T2} - 8(c_L + 2c_T)/3 + 2.231399z/2$	6.467
X_5'	$A + 2a_L - 4b_{T2} - 8(c_L + 2c_T)/3 - 1.115699z/2$	-0.266
M_5'	$A - 2a_L - 4b_{T2} + 8(c_L + 2c_T)/3 + 0.6165696z/2$	-0.360
M_2'	$A + 2a_L - 4a_T - 4(b_L + b_{T1}) + 4b_{T2} + 8(c_L + 2c_T)/3 - 1.23314z/2$	0.103
R_{15}	$A - 2a_L - 4a_T + 4(b_L + b_{T1}) + 4b_{T2} - 8(c_L + 2c_T)/3$	0.076
$(111)\frac{\pi}{2a}$	$A - (-2(b_L - b_{T1}) + 0.41635523z/2.0)$	-0.568
$(111)\frac{\pi}{4a}$	$A + \sqrt{2}(a_L + 2a_T) + 2(b_L + b_{T1} + b_{T2}) + 0.942809(c_L + 2c_T)$ $-((-b_L + b_{T1}) - 0.942809(c_L - c_T) + 0.7953677z/2)$	-1.750

TABLE X. Parameters in the effective Hamiltonian (units of eV per unit cell).

A	18.43	a_L	39.27	C_{11}	117.9
B	2.629×10^3	a_T	-10.67	C_{12}	51.50
C	4.277×10^3	b_L	4.882	C_{44}	137.2
D	-1.658×10^5	b_{T1}	-1.391	g_0	-107.7
E	9.630×10^6	b_{T2}	-0.1434	g_1	-790.3
$\overline{Z}^{*2}/\epsilon_\infty$	12.18	c_L	-3.389	g_2	-357.09
		c_T	0.7104	f	4.48

FIGURES

FIG. 1. (a) Unit cell of the cubic perovskite compounds ABO_3 (b) Low temperature crystal structure of $PbTiO_3$. Displacements of the atoms indicated by arrows form the polar distortions of the cubic unit cell.

FIG. 2. z component of the vector-like Pb-centered lattice Wannier functions. Pb, Ti and O atoms are represented by solid squares, empty squares and circles respectively. Parameters labeling the displacement patterns correspond to the length of the displacements (arrows) of atoms for the unit value of the LWF coordinate.

FIG. 3. Normal mode dispersion of H_{eff}. Solid circles are the first principles mode eigenvalues used in the fitting. Open circles are the first principles mode eigenvalues not used in fitting the H_{eff}, which test the validity of the truncated form of the effective Hamiltonian.

FIG. 4. Total energies for uniformly distorted configurations ($\vec{\xi_i} = \vec{\xi}$) along directions $(001), (110)$ and (111). Solid lines are the fit obtained with the parameters B, C, D and E in H_{eff}.

FIG. 5. Energetics of the homogeneous strain ((a) isotropic, (b) uniaxial and (c) shear) and its coupling to the uniform polar distortions. Circles are the total energies for the strained unit cell configurations with no polar distortions. Solid lines going through the circles are the fits obtained with the elastic constants C_{11}, C_{12} and C_{44}. Squares correspond to the second derivative of the total energies with respect to uniform polar distortions for the strained unit cells. Solid lines going through the squares are the fits obtained with the coupling parameters g_0, g_1 and g_2.

FIG. 6. Model energetics of the uniform polar distortions along $(100), (110)$ and (111). Dotted lines correspond to the polar distortions with the unstrained cubic unit cell, and solid lines to the distortions with unit cell allowed to relax with respect to homogeneous strain.

FIG. 7. Bounds on the transition temperature T_c as a function of system size used in the simulations.

FIG. 8. Averages of largest, smallest and intermediate absolute values of the cartesian components of the order parameter $\vec{\xi} = \sum_i \vec{\xi}_i/N$ as a function of temperature, obtained from Monte Carlo simulations (125000 mcs) of a $7 \times 7 \times 7$ system.

FIG. 9. Average tetragonal strain parameter $\frac{c}{a}$ as a function of temperature, obtained from Monte Carlo simulations (125000 mcs) of a $7 \times 7 \times 7$ system.

FIG. 10. Average unit cell volume as a function of temperature, obtained from Monte Carlo simulations (125000 mcs) of a $7 \times 7 \times 7$ system.

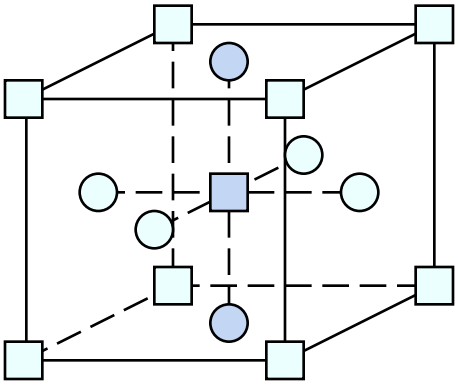

(a)

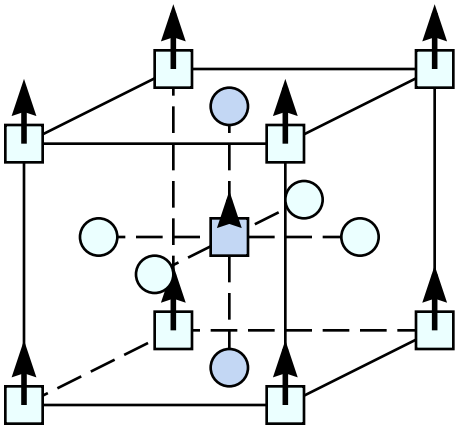

(b)

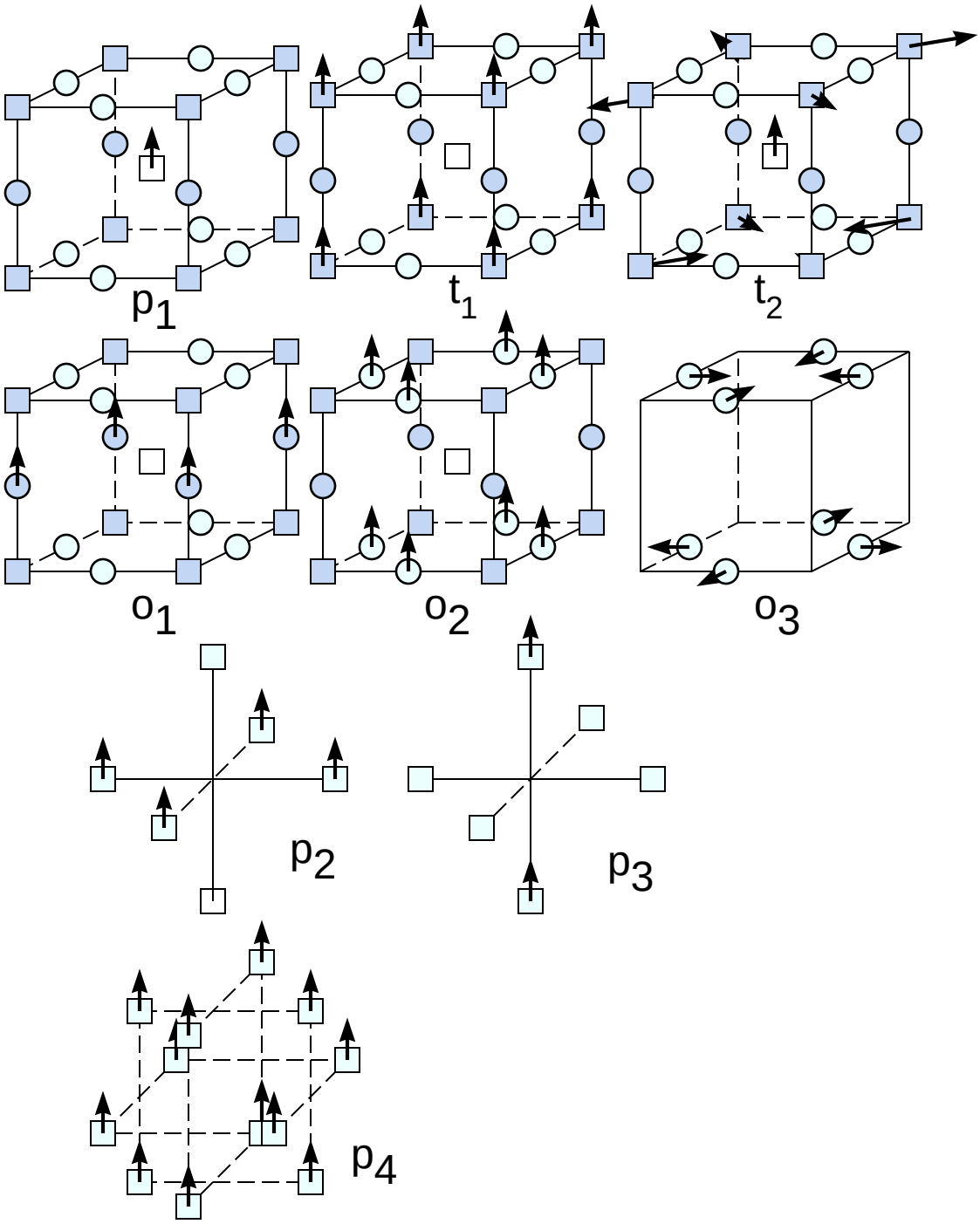
p1
t1
t2
o1
o2
o3
p2
p3
p4

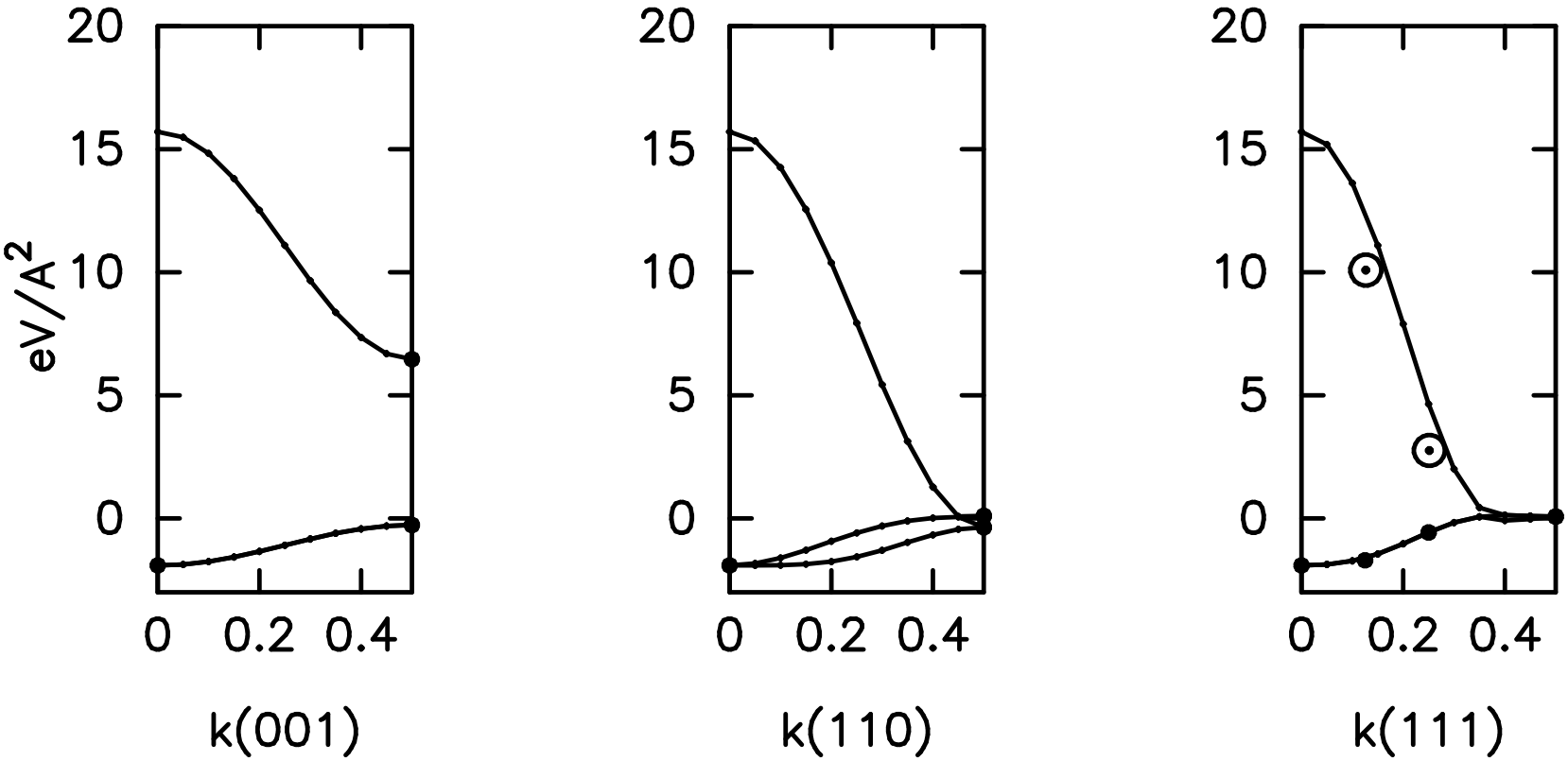
20
15
10
5
0
eV/A2
0
0.2
0.4
k(001)
20
15
10
5
0
0
0.2
0.4
k(110)
20
15
10
5
0
0
0.2
0.4
k(111)

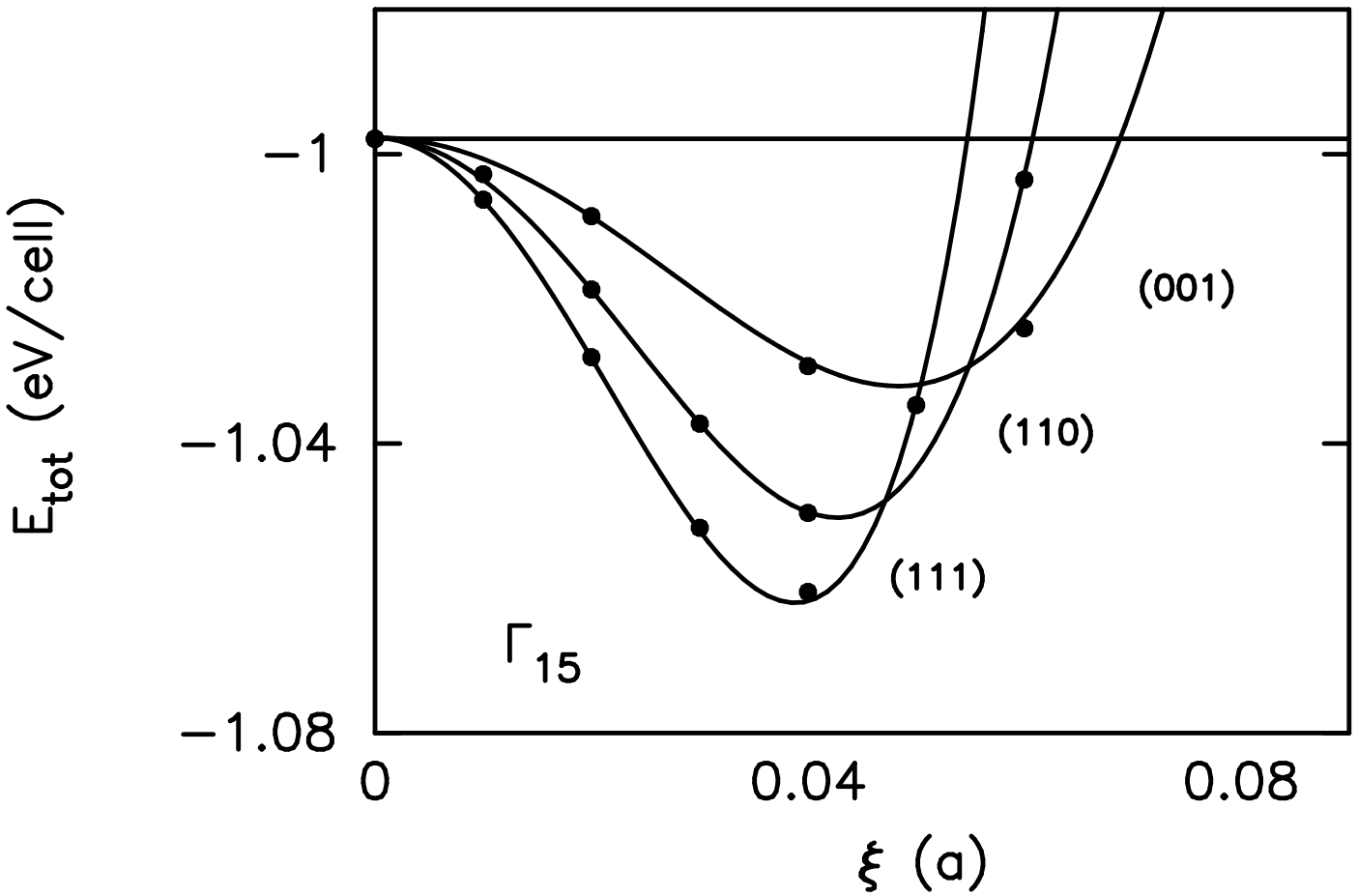
−1
−1.04
−1.08
E_{tot} (eV/cell)
0
0.04
0.08
ξ (a)
(001)
(110)
(111)
Γ_{15}

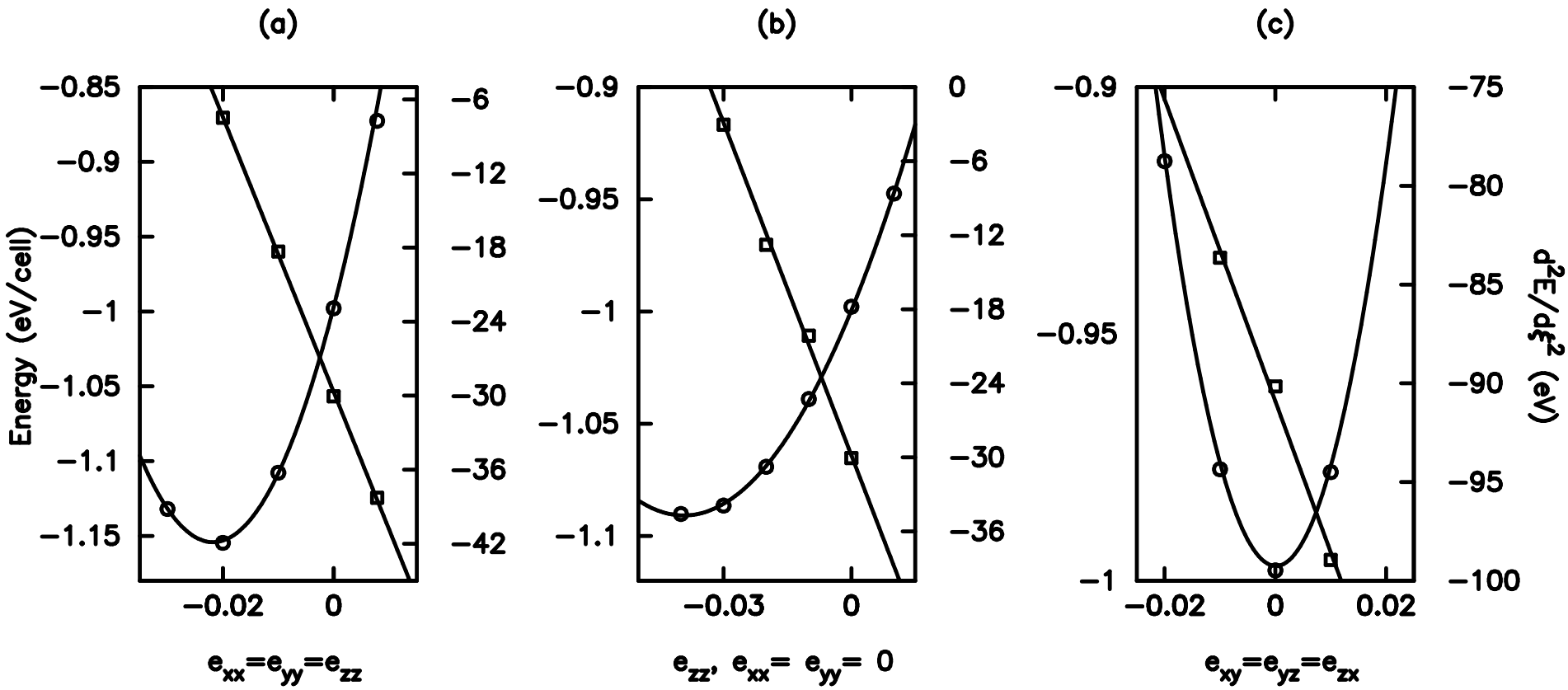
(a)
(b)
(c)
Energy (eV/cell)
d²E/dξ² (eV)
−0.85
−0.9
−0.95
−1
−1.05
−1.1
−1.15
−6
−12
−18
−24
−30
−36
−42
−0.02
0
−0.9
−0.95
−1
−1.1
0
−6
−12
−18
−24
−30
−36
−0.03
0
−0.9
−0.95
−1
−75
−80
−85
−90
−95
−100
−0.02
0
0.02
e_xx=e_yy=e_zz
e_zz, e_xx= e_yy= 0
e_xy=e_yz=e_zx

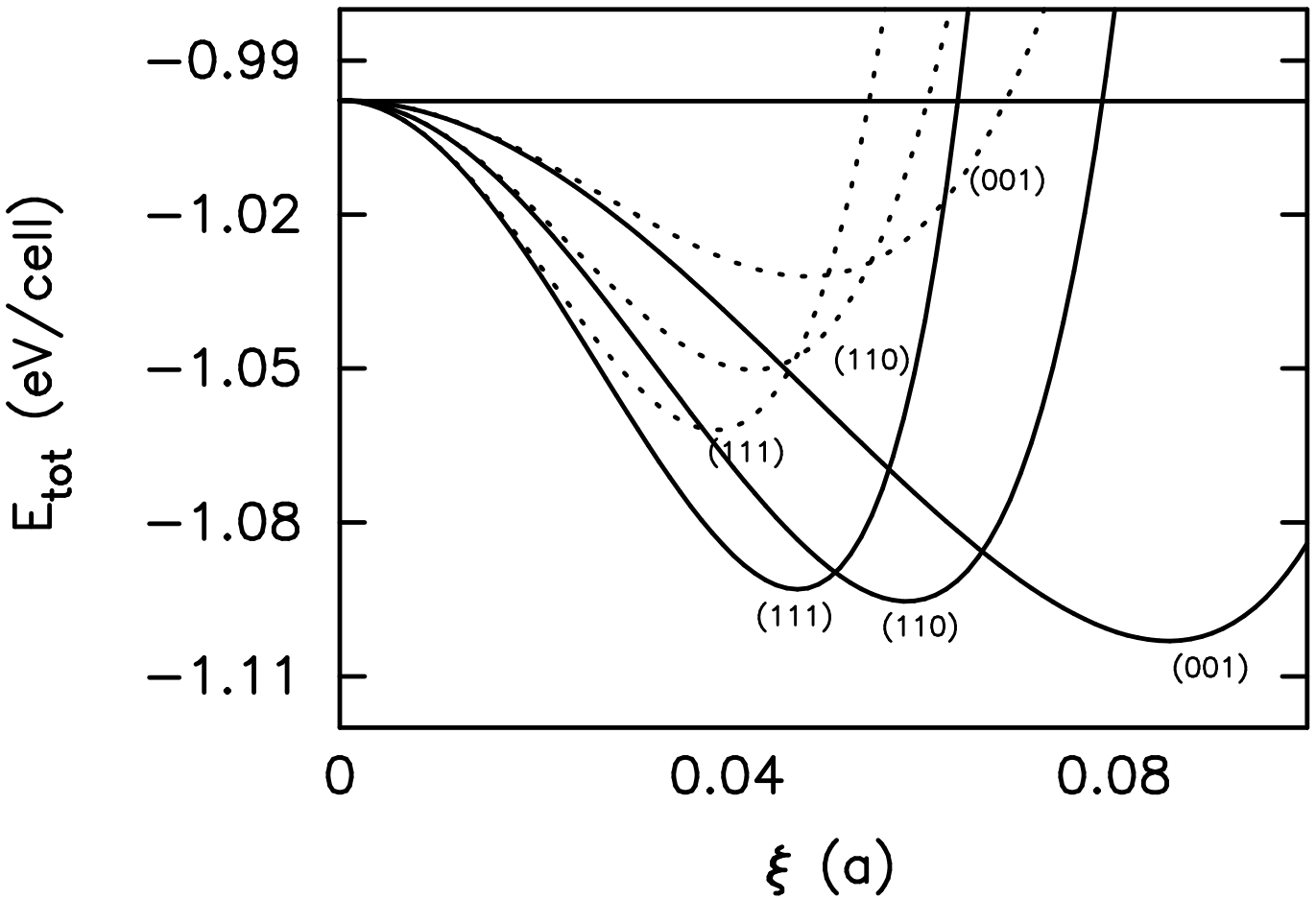
−0.99
−1.02
−1.05
−1.08
−1.11
E_{tot} (eV/cell)
0
0.04
0.08
ξ (a)
(001)
(110)
(111)
(111)
(110)
(001)

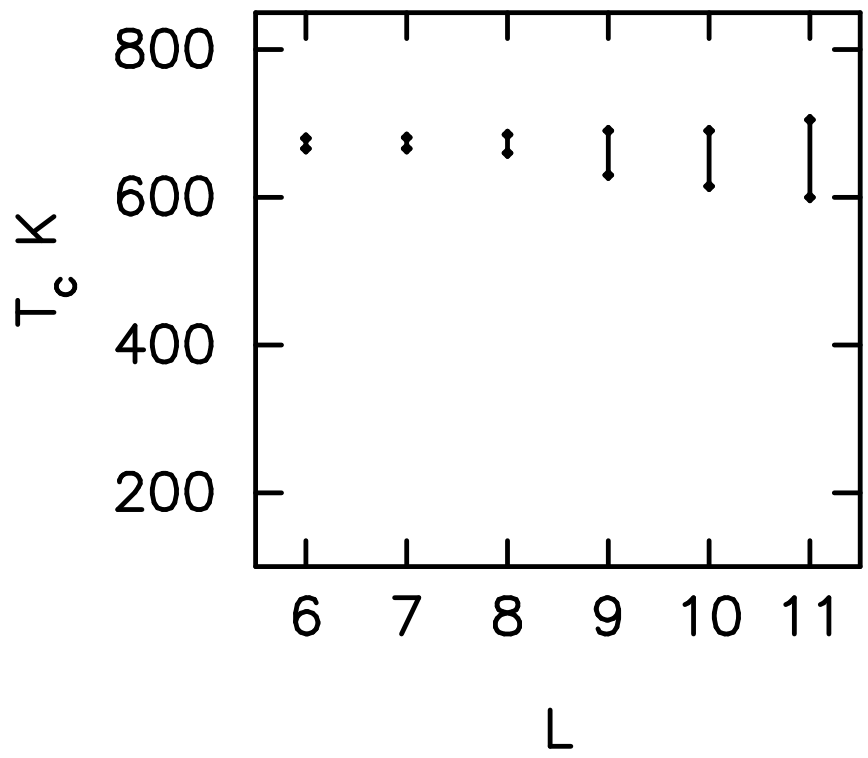
800
600
400
200
T_c K
6
7
8
9
10
11
L

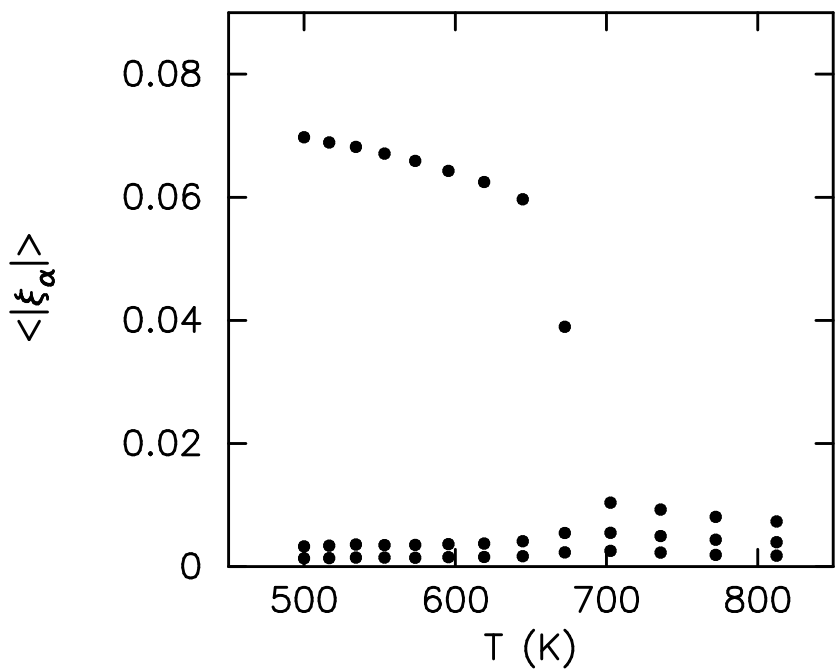
0.08
0.06
0.04
0.02
0
500
600
700
800
T (K)
<|ξα|>
0.08
0.06
0.04
0.02
0
500
600
700
800
T (K)
<|ξα|>

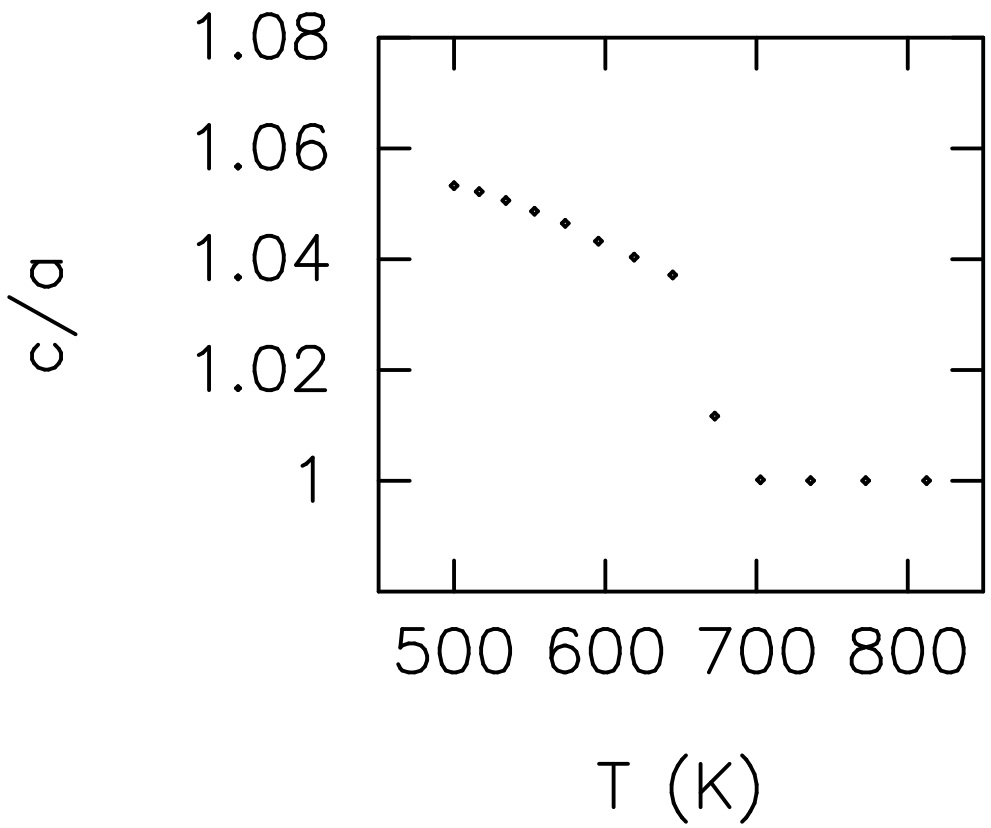
1.08
1.06
1.04
1.02
1
c/a
500 600 700 800
T (K)

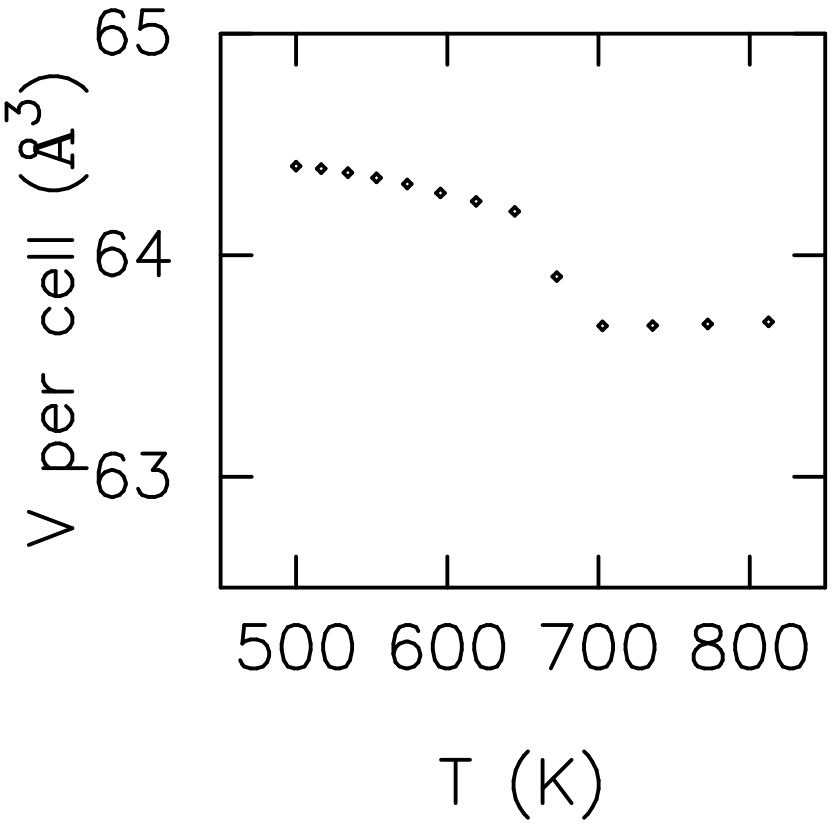
65
64
63
V per cell (Å3)
500 600 700 800
T (K)